# Stokes Flow in an Elastic Tube – A Large-Displacement Fluid-Structure Interaction Problem

In print in:
International Journal for Numerical Methods in Fluids

Matthias Heil *
Fluid Mechanics Laboratory
Massachusetts Institute of Technology
USA

February 13, 1998

**Abstract**

Viscous flow in elastic (collapsible) tubes is a large-displacement fluid-structure interaction problem frequently encountered in biomechanics. This paper presents a robust and rapidly converging procedure for the solution of the steady three-dimensional Stokes equations, coupled to the geometrically non-linear shell equations which describe the large deformations of the tube wall. The fluid and solid equations are coupled in a segregated method whose slow convergence is accelerated by an extrapolation procedure based on the scheme's asymptotic convergence behaviour. A displacement control technique is developed to handle the system's snap-through behaviour. Finally, results for the tube's post-buckling deformation and for the flow in the strongly collapsed tube are shown.

**Keywords:**

Fluid-Structure Interaction, Flow in Collapsible Tubes, Stokes Equations, Large-Displacement Shell Theory, Finite Elements.

## 1 Introduction

The efficient solution of large-displacement fluid-structure interaction problems is still a challenging problem in computational mechanics, especially if the system under consideration is three-dimensional. Numerous applications exist in offshore engineering[1], aeroelasticity[2] and bio-fluid mechanics. The problem considered in this paper is that of steady viscous flow in an elastic vessel – a model problem applicable to a wide variety of flows in the human body in which many fluid conveying vessels are elastic and deform substantially in response to the traction exerted on them by the flow.

Previous computational studies investigated the effect of wall elasticity on the flow in the arteries and in arterial bifurcations[3,4,5,6]. Such computational analyses are facilitated by the fact that the transmural pressure (internal minus external pressure) in these vessels is usually positive. Hence, the arteries tend to be inflated and they maintain their original nearly axisymmetric shape throughout the deformation. The magnitude of the deformations tends to be moderate since the vessels have a high extensional stiffness.

There are, however, numerous examples of fluid conveying vessels in the human body which are subject to a negative (compressive) transmural pressure (e.g. the veins above the level of the heart, the veins and arteries during sphygmomanometry, the airways during forced expiration). When the compressive transmural pressure on these vessels exceeds a certain critical value, the vessels buckle non-axisymmetrically. Since the vessels' structural stiffness is greatly reduced after the buckling, the changes in the tube geometry are typically quite large. Therefore, the interaction between fluid and solid mechanics tends to be very strong.

*Present Address: Department of Applied Mathematics and Theoretical Physics, University of Cambridge, U.K.

Simple one-dimensional models which were developed to analyse the problem fail to describe many of the important features, especially the system's snap-through behaviour under a variety of parameter variations.

The problem has been studied experimentally by many authors [for a more detailed review of experiments and of previous one-dimensional models see e.g. reference 7] and the typical experimental setup, shown in Fig. 1, forms the basis for most theoretical analyses: inside a pressure chamber, a thin elastic tube (typically made of rubber) of length $L$, undeformed radius $R_0$ and wall thickness $h$ is mounted on two rigid tubes. The chamber pressure, $p_{ext}$, can be prescribed independently of the fluid pressure. Viscous fluid is pumped through the tube at a steady flow rate (volume flux $\dot{V}$). In the experiments the non-axisymmetric collapse of the tube is often followed by large amplitude self-excited oscillations.

In order to develop a rational model of the problem while avoiding the complexities and computational requirements of a fully three-dimensional computation, several authors[8,9,10,11,12,13] recently examined the two-dimensional equivalent of the collapsible tube problem: the zero (or finite) Reynolds number steady (or unsteady) flow in a two-dimensional channel in which part of one wall is replaced by an elastic membrane. These studies provided a detailed picture of the fluid and solid mechanics involved in the large amplitude self-excited oscillations in this simplified system.

In another series of studies[14,15,16,17] the steady deformations of the fully coupled three-dimensional system were investigated: the tube wall was modelled as a circular cylindrical shell and geometrically non-linear shell theory was used to model its large non-axisymmetric post-buckling deformation. The fluid flow was modelled using lubrication theory (assuming low Reynolds numbers and a small wall slope in the direction of the flow). The coupled fluid-solid problem was solved using a parallelised Newton-Raphson technique based on a Finite Element discretisation of the fluid and solid equations. The results revealed many features which are unique to the three-dimensional geometry (snap-through buckling of the tube wall, flow division into the two lobes which remain open during the buckling, buckling with higher circumferential wavenumbers for increased upstream pressure, etc.). This model provides a very accurate description of the tube's deformation but some of the assumptions used in the simplification of the fluid equations were violated (after the buckling, the wall slope at the downstream end tends to be quite large).

In order to develop the first entirely self-consistent model of the flow of viscous fluid in a collapsible tube, the small slope assumption was abandoned and lubrication theory was replaced by a solution of the Stokes equations which describe the flow in arbitrary geometries at zero Reynolds number. This paper describes the computational technique developed to solve this fully coupled large-displacement fluid-structure interaction problem.

# 2 Computational Technique

Before giving details of the computational technique used in this study, we will outline the overall strategy and discuss possible alternative solution techniques. The fluid and solid equations will be discretised using Finite Element methods. The large wall displacements require the use of Lagrangian coordinates for the solid mechanics. In this formulation the computational domain for the solid equations remains fixed. The fluid equations are based on an Eulerian description, hence the fluid mesh has to be adjusted by means of an automatic mesh generator as the tube wall deforms. The solution of the fluid equations determines the fluid pressure and velocity fields from which the fluid traction on the tube wall is obtained. The combination of the fluid traction with the external pressure determines the load terms in the solid equations. Given these load terms, the solid equations can be solved to find the wall's corresponding equilibrium position.

Ideally, the fluid and solid equations would be solved simultaneously, using a global Newton-Raphson technique [as in references 9, 12, 18 or – in a modified form – in references 15 and 16]. However, the memory requirements for the storage of the global Jacobian matrix are prohibitive – even for 'pure' fluid computations[19]. Pre-conditioned conjugate gradient solvers incorporated into the Uzawa scheme provide an efficient procedure to solve the Stokes equations without storing the system matrix. However, the convergence of most iterative solvers relies heavily on the properties of the system matrix. Unfortunately, the coupled system matrix for the fluid and solid equations is neither symmetric nor positive definite. More general iterative solvers like GMRES tend to perform poorly unless a good pre-conditioner can be found – this is not an easy task for the complicated coupled system matrix. Hence, the simultaneous solution of the fluid and solid equations does not appear promising.

The scheme used in the present computations is the segregated solution procedure used previously by other authors[10,11,13]: start with an initial guess for the wall deformation; solve the fluid equations in the corresponding fluid domain; compute the fluid traction; use the fluid traction as the load term in the solid equations; compute the corresponding equilibrium wall deformation; update the fluid domain and iterate until convergence. In this scheme, the fluid and solid equations are only loosely coupled which makes it easy

to use the most appropriate solution techniques for each individual sub-problem (Uzawa scheme for the fluid equations, direct Newton-Raphson solver for the solid equations). However, the convergence of this iterative scheme tends to be very slow and – even more worrying – convergence cannot be guarenteed a priori, even if a good initial guess can be provided. Furthermore, the strongly non-linear behaviour of the coupled fluid-solid system gives rise to additional computational difficulties such as the convergence problems caused by the snap-through behaviour frequently displayed by shell structures.

The development of a fast and robust solver for this problem will be presented in the following sections. Section 2.1 gives a brief summary of the shell theory used to model the wall deformation and describes the Finite Element technique used to discretise the shell equations. Section 2.2 describes the Finite Element solution of the Stokes equations and Section 2.3 gives details of the coupling between the fluid and solid domains. In Section 2.4, the scheme's convergence characteristics are analysed and an acceleration technique is developed. Results of the computations are presented in Section 3 and the concluding section discusses possible future extensions of the coupled solver.

## 2.1 Shell Equations

We model the flexible tube of length $L$, undeformed radius $R_0$ and wall thickness $h$ as a cylindrical shell and describe its deformation using the geometrically non-linear Kirchhoff-Love type shell theory used in reference 16. The deformation of the shell is expressed in terms of the dimensionless midplane displacements $\mathbf{v} = \mathbf{v}^*/R_0$. The superscript star distinguishes dimensional quantities from their non-dimensional equivalents. We use Lagrangian coordinates $\zeta^\alpha = \zeta^{*\alpha}/R_0$ (Greek and Latin indices have values 1,2 and 1,2,3, respectively, and the summation convention is used) to parameterise the shell's midplane such that the non-dimensional vector to the undeformed midplane, $\mathbf{r}^0 = \mathbf{r}^{*0}/R_0$, is given by:

$$\mathbf{r}^0 = \left(\sin(\zeta^2), \cos(\zeta^2), \zeta^1\right)^T, \quad \zeta^1 \in [0, L/R_0], \quad \zeta^2 \in [0, 2\pi]. \tag{1}$$

Then the position of a material point at a non-dimensional distance $\zeta^3 = \zeta^{*3}/R_0$ from the shell's undeformed midplane is given by

$$\mathbf{r} = \mathbf{r}^0 + \zeta^3 \mathbf{n}, \qquad \zeta^3 \in [-h/(2R_0), h/(2R_0)], \tag{2}$$

where $\mathbf{n} = \left(\sin(\zeta^2), \cos(\zeta^2), 0\right)^T$ is the vector normal to the undeformed midplane; see Fig. 2.

After the deformation, the material point on the midplane with the Lagrangian coordinates $\zeta^\alpha$ has been displaced to a new position $\mathbf{R}^0(\zeta^\alpha) = \mathbf{r}^0(\zeta^\alpha) + \mathbf{v}(\zeta^\alpha)$. We decompose the displacement vector $\mathbf{v}$ into the undeformed basis, $\mathbf{v} = v^j\ \mathbf{a}_j$, where the undeformed base vectors are given by $\mathbf{a}_\alpha = \mathbf{r}^0_{,\alpha}$ and $\mathbf{a}_3 = \mathbf{n}$. The comma denotes the partial derivative with respect to the Lagrangian coordinates. Lowercase and uppercase letters are used for shell variables associated with the undeformed and deformed geometry, respectively.

The Kirchhoff-Love assumption states that material lines which were normal to the undeformed midplane remain normal to the shell's midplane thoughout its deformation and that they remain unstretched. Therefore, the vector to an arbitrary material point in the shell after the deformation is given by

$$\mathbf{R} = \mathbf{R}^0 + \zeta^3\ \mathbf{N}, \tag{3}$$

where $\mathbf{N}$ is the vector normal to the deformed shell.

In spite of the large deformations, the strain is typically fairly small which allows Hooke's law to be used as the constitutive equation. Then the principle of virtual displacements which governs the shell's deformation is given by

$$\int_0^{2\pi}\int_0^{L/R_0} \left[E^{\alpha\beta\gamma\delta}\left(\gamma_{\alpha\beta}\ \delta\gamma_{\gamma\delta} + \frac{1}{12}\left(\frac{h}{R_0}\right)^2 \kappa_{\alpha\beta}\ \delta\kappa_{\gamma\delta}\right) - \left(\frac{R_0}{h}\right)(\mathbf{f}\cdot\delta\mathbf{R})\,|_{\zeta^3=\pm h/(2R_0)}\right]\ d\zeta^1\ d\zeta^2 = 0, \tag{4}$$

where $\mathbf{f} = \mathbf{f}^*/E$ is the traction per unit area of the undeformed midplane, non-dimensionalised with Young's modulus $E$. $\gamma_{\alpha\beta}$ and $\kappa_{\alpha\beta}$ are the non-dimensional strain and bending tensors (given in the appendix) and the dimensionless plane stress stiffness tensor, $E^{\alpha\beta\gamma\delta} = E^{*\alpha\beta\gamma\delta}/E$ is given by

$$E^{\alpha\beta\gamma\delta} = \frac{1}{2(1+\nu)}\left(\delta^{\alpha\gamma}\delta^{\beta\delta} + \delta^{\alpha\delta}\delta^{\beta\gamma} + \frac{2\nu}{1-\nu}\delta^{\alpha\beta}\delta^{\gamma\delta}\right), \tag{5}$$

where $\nu$ is Poisson's ratio.

The variations of strain and bending tensor have to be taken with respect to the displacements $v^i$ and their derivatives. The tube is clamped at both ends. Therefore, at $\zeta^1 = 0$ and $\zeta^1 = L/R_0$ the displacements

have to be prescribed and we have $dv^3/d\zeta^1 = 0$. A more detailed discussion of the large-displacement shell theory can be found in reference 20.

Since a variational equation exists for the solid mechanics, we choose a displacement based Finite Element technique to discretise the equations. Carrying out the variations in (4) is a straightforward process but involves some lengthy algebra. The computer algebra package MAPLE was used to express (4) in terms of the displacements and their derivatives, giving

$$\int_0^{2\pi} \int_0^{L/R_0} \left( \phi_i \ \delta v^i + \phi_{i\alpha} \ \delta v^i_{,\alpha} + \phi_{i\alpha\beta} \ \delta v^i_{,\alpha\beta} \right) \ d\zeta^1 \ d\zeta^2 = 0. \tag{6}$$

The $\phi$ terms contain up to second derivatives of the displacements, therefore we need shape functions with continuous first derivatives across the element boundaries. Quadrilateral isoparametric Hermite elements with nodal displacements and slopes as independent degrees of freedom[21] were chosen. Within element number $\mathcal{E}$ ($\mathcal{E} = 1, N_s$, where $N_s$ is the total number of shell elements) the displacements $v^i$ were interpolated as

$$v^i = \sum_{j,k=1}^{4} V^{iJ(j,\mathcal{E})k} \psi_{jk}(s_1, s_2) \quad s_\alpha \in [0, 1]. \tag{7}$$

The shape functions were chosen to be tensor products of the one-dimensional Hermite polynomials $h_1(s) = 2s^3 - 3s^2 + 1$, $h_2(s) = s^3 - 2s^2 + s$, $h_3(s) = -(2s^3 - 3s^2)$ and $h_4(s) = s^3 - s^2$. The first index of the shape function $\psi_{jk}$ stands for the local node number ($j = 1, 4$). The shape function's second index ($k = 1, 4$) stands for the type of the degree of freedom (interpolating the displacement, the two first derivatives or the mixed second derivative with respect to the local coordinates); $J(j, \mathcal{E})$ represents the global node number of local node $j$ in element $\mathcal{E}$.

To generate isoparametric elements, the same shape functions were used to map the local coordinates $(s_1, s_2)$ to the global coordinates $(\zeta^1, \zeta^2)$,

$$\zeta^\alpha = \sum_{j,k=1}^{4} Z^{\alpha J(j,\mathcal{E})k} \psi_{jk}(s_1, s_2), \tag{8}$$

Details of the choice of the coefficients $Z^{\alpha J(j,\mathcal{E})k}$ are given in reference 16.

The tube's buckled configuration is symmetric and for the relatively long tubes considered here, the most unstable buckling mode has two circumferential waves[14], as sketched in Fig. 1. Therefore, only one quarter of the tube needs to be discretised.

We insert (7) and (8) into (6) and obtain

$$\sum_{\mathcal{E}=1}^{N_s} \sum_{j,k=1}^{4} \left\{ \int_0^1 \int_0^1 \left( \phi_i \ \psi_{jk} + \phi_{i\alpha} \ \psi_{jk,\alpha} + \phi_{i\alpha\beta} \ \psi_{jk,\alpha\beta} \right) \ \mathcal{J} \ ds_1 \ ds_2 \right\} \delta V^{iJ(j,\mathcal{E})k} = 0, \tag{9}$$

where $\mathcal{J}$ is the determinant of the Jacobian of the mapping between the local coordinates $(s_1, s_2)$ and the global coordinates $(\zeta^1, \zeta^2)$. The variations of those $V^{ijk}$ which are not determined by the boundary conditions are arbitrary. This leads to the following set of nonlinear algebraic equations $f_{ijk}$ for the unknown $V^{ijk}$:

$$f_{ijk} = \sum_{\mathcal{E}=1}^{N_s} \int_0^1 \int_0^1 \left\{ \left( \phi_i \ \psi_{lk} + \phi_{i\alpha} \ \psi_{lk,\alpha} + \phi_{i\alpha\beta} \ \psi_{lk,\alpha\beta} \right)|_{J(l,\mathcal{E})=j} \ \mathcal{J} \right\} \ ds_1 \ ds_2 = 0. \tag{10}$$

These equations still contain the load terms, which have to be determined from the solution of the fluid equations. The double integral over the elements was evaluated using a 3×3 Gaussian integration. Therefore, the load terms only need to be determined at the Gauss points within each element. The above set of equations was solved using a Newton-Raphson method. Since the exact expressions for strain and bending tensor have to be used[16], the integrand in (10) contains very complex algebraic expressions. Therefore, it is computationally more efficient to determine the Jacobian matrix by finite differencing than to use the analytical expressions for its coefficients. The linear systems were solved using LU-decomposition since the presence of follower loads and the displacement control technique (described below) make the system matrix non-symmetric.

## 2.2 Fluid Equations

For sufficiently low Reynolds number the Navier-Stokes equations, which govern the fluid flow, can be approximated by the linear Stokes equations given in dimensionless form by

$$\frac{\partial p}{\partial x_i} = \bar{\mu}\ \frac{\partial^2 u_i}{\partial x_j^2} \tag{11}$$

and the continuity equation

$$\frac{\partial u_i}{\partial x_i} = 0, \tag{12}$$

where

$$\bar{\mu} = \frac{\mu U}{R_0 E} \tag{13}$$

and $\mu$ is the dynamic viscosity of the fluid. In (11) and (12) the velocities were non-dimensionalised with the average velocity through the tube, $u_i = u_i^*/U$, where $U = \dot{V}/(\pi R_0^2)$, and Young's modulus was used to non-dimensionalise the pressure, $p = p^*/E$. The cartesian coordinates $x_i^*$ were non-dimensionalised with the undeformed tube radius, $x_i = x_i^*/R_0$.

The fluid traction acting on the tube wall is given by

$$f_i = pN_i - \bar{\mu}\left(\frac{\partial u_i}{\partial x_j} + \frac{\partial u_j}{\partial x_i}\right) N_j, \tag{14}$$

where the $N_i$ are the cartesian components of the normal vector, $\mathbf{N}$, on the tube wall.

We transform the Stokes equation into their weak form by multiplying the momentum and continuity equations by test functions $\Psi^F$ and $\Psi^C$, respectively, and integrating them by parts. This yields

$$\int \left(-p\frac{\partial \Psi^F}{\partial x_i} + \bar{\mu}\frac{\partial u_i}{\partial x_j}\frac{\partial \Psi^F}{\partial x_j}\right) dV = \oint \left(-pn_i + \bar{\mu}\frac{\partial u_i}{\partial n}\right) \Psi^F dA \tag{15}$$

and

$$\int \left(-\Psi^C \frac{\partial u_j}{\partial x_j}\right) dV = 0, \tag{16}$$

where the volume and area integrals have to be taken over the fluid domain $V$ and its boundary $A$, respectively.

We discretise the weak equations with $N_f$ isoparametric Taylor-Hood type brick shaped Finite Elements. The velocities and pressures within fluid element $\mathcal{E}$ ($\mathcal{E} = 1, N_f$) are thus interpolated as

$$u_i = \sum_{j=1}^{27} U^{iJ_f(j,\mathcal{E})}\ \psi_j^F(s_1, s_2, s_3) \tag{17}$$

and

$$p = \sum_{j=1}^{8} P^{J_p(j,\mathcal{E})}\ \psi_j^P(s_1, s_2, s_3), \tag{18}$$

respectively. The isoparametric mapping between local and global coordinates uses the velocity shape functions, i.e.

$$x_i = \sum_{j=1}^{27} X^{iJ_f(j,\mathcal{E})}\ \psi_j^F(s_1, s_2, s_3), \tag{19}$$

where the $X^{ij}$ are the $x_i$ coordinates of the global node $j$.

The three-dimensional velocity and pressure shape functions are tensor products of the one-dimensional quadratic and linear Lagrangian interpolants $L_{u1}(s) = s(s-1)/2$, $L_{u2}(s) = (s+1)(s-1)/2$, $L_{u3}(s) = s(s+1)/2$ and $L_{p1}(s) = -(s-1)/2$, $L_{p2}(s) = (s+1)/2$, respectively, where $s \in [-1, 1]$. $J_f(j, \mathcal{E})$ and $J_p(j, \mathcal{E})$ are the global velocity and pressure node numbers of the local node $j$ in fluid element $\mathcal{E}$. Choosing the test functions $\Psi^F$ and $\Psi^C$ in the momentum and continuity equations to be the velocity and pressure shape functions, respectively, transforms the volume integrals in (15) and (16) into the following set of linear

equations

$$f_{ik}^F = \sum_{\mathcal{E}=1}^{N_f} \int_{-1}^{1}\int_{-1}^{1}\int_{-1}^{1} \left[ -\sum_{j_p=1}^{8} \psi_{j_p}^P \, \frac{\partial \psi_l^F}{\partial x_i} \, P^{J_p(j_p,\mathcal{E})} \right.$$

$$\left. +\bar{\mu} \sum_{j_f=1}^{27} \frac{\partial \psi_{j_f}^F}{\partial x_n} \frac{\partial \psi_l^F}{\partial x_n} U^{iJ_f(j_f,\mathcal{E})} \right] \Bigg|_{J_f(l,\mathcal{E})=k} \mathcal{J}_F \; ds_1 ds_2 ds_3 = 0, \tag{20}$$

where $i = 1, 3$; $k = 1, M_f$ and

$$f_k^P = \sum_{\mathcal{E}=1}^{N_f} \int_{-1}^{1}\int_{-1}^{1}\int_{-1}^{1} \left[ \sum_{j_f=1}^{27} -\frac{\partial \psi_{j_f}^F}{\partial x_i} \, \psi_l^P \, U^{iJ_f(j_f,\mathcal{E})} \right] \Bigg|_{J_p(l,\mathcal{E})=k} \mathcal{J}_F \; ds_1 ds_2 ds_3 = 0, \tag{21}$$

where $k = 1, M_p$. $M_f$ and $M_p$ are the total number of velocity and pressure nodes and $\mathcal{J}_F$ is the determinant of the Jacobian of the isoparametric mapping (19). The minus sign in the discretised continuity equation was introduced to make the system symmetric. The integrals were evaluated numerically with a $3 \times 3$ Gauss rule.

The tube's deformation is symmetric, therefore we discretise only one quarter of the fluid domain and apply the following boundary conditions: (i) at the tube's upstream end we prescribe a fully developed parabolic velocity profile, $u_\alpha = 0$, $u_3 = 2\,[1 - (x_1^2 + x_2^2)/(1 - \frac{h}{2R_0})^2]$; (ii) at the tube's downstream end we impose normal outflow, $u_\alpha = 0$, and $-p + \bar{\mu}\, \partial u_3/\partial x_3 = 0$ which sets the pressure to zero; (iii) at the symmetry boundaries we set the normal velocities and the tangential shear stresses to zero (e.g. at $x_1 = 0$: $u_1 = 0$, $\partial u_2/\partial x_1 = \partial u_3/\partial x_1 = 0$); (iv) on the rigid walls we apply the no-slip condition $u_i = 0$. With these boundary conditions the surface integral in (15) vanishes everywhere and after applying the Dirichlet velocity boundary conditions, the linear equations (20) and (21) fully determine the unknown velocity and pressure variables. Symbolically, the equations (20) and (21) can be written as

$$\begin{bmatrix} \underline{\mathbf{A}}_1 & \underline{\mathbf{0}} & \underline{\mathbf{0}} & -\underline{\mathbf{D}}_1^T \\ \underline{\mathbf{0}} & \underline{\mathbf{A}}_2 & \underline{\mathbf{0}} & -\underline{\mathbf{D}}_2^T \\ \underline{\mathbf{0}} & \underline{\mathbf{0}} & \underline{\mathbf{A}}_3 & -\underline{\mathbf{D}}_3^T \\ -\underline{\mathbf{D}}_1 & -\underline{\mathbf{D}}_2 & -\underline{\mathbf{D}}_3 & \underline{\mathbf{0}} \end{bmatrix} \begin{pmatrix} \mathbf{u}_1 \\ \mathbf{u}_2 \\ \mathbf{u}_3 \\ \mathbf{p} \end{pmatrix} = \begin{pmatrix} \mathbf{f}_1 \\ \mathbf{f}_2 \\ \mathbf{f}_3 \\ \mathbf{f}_p \end{pmatrix}, \tag{22}$$

where the $\underline{\mathbf{A}}_i$ are the symmetric positive definite matrices resulting from the Finite Element discretisation of the Laplace operator in the $i$-th momentum equation and the $\underline{\mathbf{D}}_i^T$ and $\underline{\mathbf{D}}_i$ are the discretised gradient and divergence operators, respectively. The vectors $\mathbf{u}_i$ and $\mathbf{p}$ contain the unknown velocity and pressure values and the right hand side vector contains the contributions due to the Dirichlet boundary conditions.

The equations were solved using the classical Uzawa scheme[22], operating on the equation

$$\sum_{i=1}^{3} \underline{\mathbf{D}}_i \underline{\mathbf{A}}_i^{-1} \underline{\mathbf{D}}_i^T \mathbf{p} = -\mathbf{f}_p - \sum_{i=1}^{3} \underline{\mathbf{D}}_i \underline{\mathbf{A}}_i^{-1} \mathbf{f}_i, \tag{23}$$

which is obtained by block elimination from (22). A preconditioned conjugate gradient solver is used to solve equation (23) for the pressure unknowns (see Appendix B for details). Once the pressure is determined, the velocities are obtained from the systems

$$\underline{\mathbf{A}}_{(i)} \mathbf{u}_{(i)} = \mathbf{f}_i + \underline{\mathbf{D}}_i^T \mathbf{p} \quad \text{(no summation on } i\text{)} \tag{24}$$

which were also solved with a preconditioned conjugate gradient method (the diagonal of $\underline{\mathbf{A}}_i$ was used as the preconditioner).

## 2.3 Fluid Solid Coupling

The fluid and solid solvers interact through the traction exerted by the fluid on the tube wall. Also, the fluid mesh generator has to adjust the fluid mesh in response to the wall deformation. This is achieved as follows: a structured fluid mesh is generated in the undeformed cylindrical tube. In this reference configuration, the fluid nodes on the tube wall coincide with certain material points in the shell. When the tube wall deforms, the fluid mesh is re-generated by keeping the fluid mesh 'attached' to the same material points. Hence, the wall displacement directly determines the position of the fluid nodes on the tube wall. The construction of

the mesh in the interior is illustrated in Fig. 3. The nodal points in the fluid mesh are arranged in axial layers. In each layer a central box whose dimensions are based on the local height and width of the tube is constructed. During the buckling the tube wall warps slightly. The warping displaces material points on the wall which had the same $x_3$ coordinate in the reference configuration to different axial positions. The central box is located at the average axial position of the corresponding nodal points on the tube wall. The edges of the elements in the region surrounding the central box are formed by straight lines to the tube wall.

As the tube collapses, the axial spacing of the fluid elements is occasionally updated to refine the fluid mesh in the region of strongest collapse. This refinement is based on the requirement that the depth of the elements (in the axial direction) in each layer be approximately equal to their average height (measured in the plane of strongest collapse).

Once the fluid equations are solved on this mesh, the fluid traction on the tube wall needs to be determined at the solid Gauss points. Let us denote the vector to the solid Gauss point $i_S$ ($i_S = 1, 9$) in the solid element $\mathcal{E}_S$ by $\tilde{\mathbf{R}}_{(i_S,\mathcal{E}_S)}$. Since different element types and isoparametric mappings were used for the fluid and solid domains, points on the boundary of the fluid domain do not necessarily coincide exactly with points on the tube wall (unless they are nodal points in the fluid mesh). This is illustrated in Fig. 4. The fluid traction for a given solid Gauss point (point A in Fig. 4) was therefore determined at the intersection of the boundary of the discretised fluid domain with the normal vector on the tube wall at the Gauss point, $\tilde{\mathbf{N}}_{(i_S,\mathcal{E}_S)}$. This point (point B in Fig. 4), whose position vector we denote by $\tilde{\mathbf{R}}^{(F)}$, is located on one of the faces of the fluid elements. Therefore, one of the local fluid coordinates of this point is known ($s_3^{(F)} = 1$ in Fig. 4). The other two local coordinates, $s_\alpha^{(F)}$ (together with the fluid element number, $\mathcal{E}^{(F)}$) and the distance $\xi$ between Gauss point and the fluid mesh are then determined from the equation

$$\tilde{\mathbf{R}}_{(i_S,\mathcal{E}_S)} + \xi\tilde{\mathbf{N}}_{(i_S,\mathcal{E}_S)} = \tilde{\mathbf{R}}^{(F)}\left(\mathcal{E}^{(F)}, s_1^{(F)}, s_2^{(F)}, s_3^{(F)} = 1\right), \tag{25}$$

which is solved using a Newton-Raphson method. The gap between the tube wall and the discretised fluid domain is $\mathbf{g} = \xi\tilde{\mathbf{N}}_{(i_S,\mathcal{E}_S)}$. Since the fluid and solid domains are very tightly coupled, the fluid coordinates corresponding to each solid Gauss point change very little during the tube's deformation and the Newton-Raphson iteration usually converges within one step.

An estimate of the errors introduced by the approximate transfer of the traction is readily obtained from a Taylor expansion. For instance, the error for the pressure is approximately

$$\delta p \approx \left|\frac{\partial p}{\partial x_i}\, g_i\right|, \tag{26}$$

where the $g_i$ are the cartesian components of the gap vector $\mathbf{g}$. The error estimates can readily be evaluated during the traction transfer. In all computations the discretisation of the fluid and solid domains was sufficiently fine to ensure that $\max|\delta p/(p_{entry} - p_{exit})| < 5.0 \times 10^{-4}$.

## 2.4 The Coupled Solution

As mentioned in the introduction, the basic iterative scheme (switching between fluid and solid solver) tends to be very slowly convergent and the computational cost can easily become prohibitive since each iteration requires the solution of a full three-dimensional Stokes problem. Furthermore, in its simplest (and easiest to implement) form the scheme does not provide any means of handling the snap-through behaviour frequently displayed by shell structures.

We will now present two modifications to the iteration scheme that increase its convergence rate dramatically and also make the overall scheme much more robust. For this purpose we introduce a slightly more abstract notation for the problem. Let us denote the discretised fluid and solid variables by $V_i$ ($i = 1, N_{Shell}$) and $U_j$ ($j = 1, N_{Fluid}$), respectively, where $N_{Shell}$ and $N_{Fluid}$ are the number of degrees of freedom in the respective domains. We write the discretised shell equations, $\mathcal{S}_i$, which depend on the displacement variables and – through the load terms $\mathbf{f}$ – on the fluid variables, as

$$\mathcal{S}_i(V_i, \mathbf{f}(U_j)) = \mathcal{S}_i(V_i, U_j) = 0, \qquad i = 1, N_{Shell} \quad j = 1, N_{Fluid}. \tag{27}$$

Similarly, the discretised fluid equations, $\mathcal{F}_j$, depend not only on the fluid variables but also on the displacement variables which determine the tube geometry and hence the nodal positions in the fluid mesh, i.e.

$$\mathcal{F}_j(V_i, U_j) = 0, \qquad i = 1, N_{Shell} \quad j = 1, N_{Fluid}. \tag{28}$$

### 2.4.1 The Continuation Technique

The strong non-linearity of the shell equations requires the use of a continuation technique to compute the displacement fields corresponding to a strongly collapsed tube. For simplicity we will first discuss the continuation technique for the simpler case of zero flow and vanishing external pressure. In this case, the load terms are given by the hydrostatic pressure on the tube wall, i.e. $\mathbf{f} = p\mathbf{N}$, where $\mathbf{N}$ is the normal vector on the tube wall. The displacement field corresponding to a large negative (compressive) pressure can readily be computed through a sequence of intermediate displacement fields corresponding to slowly increasing compressive loads. The sequence is started with a slightly buckled tube and the equilibrium displacement field for each load level is used as the initial guess for the Newton-Raphson iteration at the next level.

This basic continuation technique usually fails if the shell displays a snap-through (a sudden large change in the displacement field for a critical value of the load $p$). One way to overcome this problem is to choose a Finite Element node in the collapsing part of the tube and to prescribe its radial displacement, $V_I$, in an additional equation, i.e.

$$\mathcal{S}_{N_{Shell}+1} = V_I - \tilde{V} = 0. \tag{29}$$

If the control node is chosen such that its radial displacement increases monotonically during the tube's collapse, the continuation procedure can be based on a stepwise increase of the prescribed displacement value, $\tilde{V}$, and the pressure, $p$, can be regarded as an additional unknown[23]. The Jacobian matrix of this augmented system has the form

$$\left[\begin{array}{c|c} \left[\frac{\partial \mathcal{F}_i}{\partial V_j}\right] & \left(\frac{\partial \mathcal{F}_i}{\partial p}\right) \\ \hline 0 \ldots\ 0\ 1\ 0\ \ldots\ 0 & 0 \end{array}\right] \quad (i,j = 1, N_{Shell}). \tag{30}$$

The only non-zero entry in the last row of this matrix is in the $I$-th column, corresponding to the degree of freedom prescribed by (29). The additional column contains the derivatives of the discretised shell equations with respect to the pressure. Since the shell equations are linear in the pressure (see (4)), these are easily evaluated.

In the case of non-zero flow, the fluid traction varies through the tube and it is not possible to regard the fluid pressure as a load parameter. We can, however, make use of the fact that the incompressible Stokes equations only determine the pressure up to an arbitrary constant. This allows us to add a spatially constant pressure, $p_\delta$, to the pressure field obtained from the solution of the Stokes equations when we determine the fluid traction on the tube wall, i.e.

$$\mathbf{f} = \mathbf{f}_{Stokes} + p_\delta \mathbf{N}. \tag{31}$$

The scalar $p_\delta$ can be used as the load parameter in the displacement control technique described above. This approach corresponds to an experimental procedure in which we adjust the external pressure, $p_{ext}$, to control the tube's collapse while keeping the volume flux and the downstream fluid pressure constant.

Other experimental procedures (e.g. controlling the tube's collapse by varying the volume flux while keeping the external pressure constant) cannot be simulated directly because the derivative of the discretised shell equations with respect to the volume flux (required in the last column of the augmented Jacobian matrix) cannot be evaluated in a segregated approach. The data corresponding to such parameter variations has to be generated by interpolation.

It should be noted that the continuation technique does not ensure that the solution switches from the axisymmetric pre-buckling solution onto the post-buckled solution branch when the critical value of the control pressure is exceeded. A more sophisticated continuation technique, such as Keller's arclength method[24], would be required for this purpose. However, such branch selecting methods have to evaluate the global Jacobian matrix at the bifurcation point. This is clearly not possible in a segregated approach which was specifically designed to operate without this matrix. To force the tube onto the buckled path, a small non-axisymmetric disturbance, $p_{cos}\cos(2\zeta^2)$ with $p_{cos} \ll 1$, was therefore superimposed onto the pressure field. This disturbance made the tube buckle in the required mode shape and the value of the control displacement could be increased in small steps until opposite wall contact was detected for the first time. The last displacement field before the occurrence of opposite wall contact was then used as an initial guess for the second part of the run in which the disturbance pressure was set to zero and the control displacement was reduced until the tube was re-opened to its axisymmetric shape. Since the first part of the run merely serves to provide an initial guess for the wall shape of the strongly collapsed tube, the solver based on the lubrication theory approximation of the Stokes equations[16], which is computationally much cheaper, was used as the fluid solver for this part of the computation.

### 2.4.2 The Iteration Procedure

We will now analyse the convergence characteristics of the iteration procedure. Using the abstract notation introduced above, the procedure is given by:

**1)** Provide an initial guess for the displacement field: $n = 0, V_i^{(0)}$.

**2)** Solve $\mathcal{F}_j(V_i^{(n)}, U_j^{(n+1)}) = 0$ for $U_j^{(n+1)}$, or symbolically

$$U_j^{(n+1)} = \mathcal{F}_j^{-1}(V_i^{(n)}).$$

**3)** Solve $\mathcal{S}_i(V_i^{(n+1)}, U_j^{(n+1)}) = 0$ for $V_i^{(n+1)}$, or symbolically

$$V_i^{(n+1)} = \mathcal{S}_i^{-1}(U_j^{(n+1)}).$$

**4)** Check for convergence, i.e.

$$\delta V_{max}^{(n)} = \max_{i=1,N_{Shell}} \left| V_i^{(n+1)} - V_i^{(n)} \right| < \epsilon_{tol}.$$

**5)** Set $n := n + 1$ and go to 2).

The tolerance level for convergence, $\epsilon_{tol}$ was coupled to the value of the prescribed displacement value by setting

$$\epsilon_{tol} = 10^{-3} \times \tilde{V}. \tag{32}$$

Figure 5 shows the convergence history of an iteration based on this scheme: the radial displacements of the FEM nodes along the line of strongest collapse ($\zeta^2 = \pi/2$) are plotted against the number of iterations. The dashed line shows the displacement of the control node whose displacement was changed from $\tilde{V} = -0.8$ to $\tilde{V} = -0.7$. The displacement control technique ensures that its value is kept constant at the prescribed value. All other nodes oscillate around their final equilibrium position and 56 iterations are required to achieve a fully converged solution.

In order to analyse this convergence behaviour in a more compact form we eliminate the intermediate fluid solve and thereby condense the iteration into an iterative procedure involving only the solid variables, i.e.

$$V_i^{(n+1)} = \mathcal{S}_i^{-1}\left(\mathcal{F}_j^{-1}(V_i^{(n)})\right). \tag{33}$$

This equation shows that the procedure has the character of a Picard fixpoint iteration. Using the Taylor expansion of (33) we obtain

$$\delta V_i^{(n+1)} = \alpha_{ij}\ \delta V_j^{(n)} + O\left((\delta V_i^{(n)})^2\right) \tag{34}$$

where

$$\alpha_{ij} = \frac{\partial \mathcal{S}_i^{-1}}{\partial U_k}\frac{\partial \mathcal{F}_k^{-1}}{\partial V_j}, \qquad i,j = 1, N_{Shell}; \quad k = 1, N_{Fluid} \tag{35}$$

and $\delta V_i^{(n)} = V_i^{(n+1)} - V_i^{(n)}$. The scheme converges only if the spectral radius of $\alpha_{ij}$ is less than one. It is impractical to check the scheme's convergence in this way as the the coefficients $\alpha_{ij}$ are very expensive to compute. They also have to be evaluated 'near' the converged solution, which is not known a priori. However, the asymptotic equation (34) can be exploited to accelerate the procedure *if* it converges.

From (34) it is evident that the increment in each displacement variable is affected by the increments in all other displacement variables during the previous iteration. A more detailed examination of the successive displacement fields during the iteration reveals that this is an overly pessimistic estimate. Figure 6 shows the deformation of the two symmetry lines on the tube wall (at $\zeta^2 = 0$ and $\zeta^2 = \pi/2$) as the iteration proceeds. The dashed lines are the initial guesses, the solid lines are the converged solutions and the dotted lines represent the intermediate wall shapes. Figure 6 shows that the displacement control technique has a very positive side effect: since a nodal point in the interior of the shell has been pinned at a fixed position, the shell is forced to pivot around this point. As the iteration proceeds, the successive tube shapes approach the equilibrium position in a damped oscillation with approximately constant mode shapes (see Fig. 6) and geometrically decreasing amplitudes (see Fig. 5) . If the displacement control technique is disabled, the tube usually either re-opens until it reaches an axisymmetric shape or it collapses so strongly that the opposite walls come into contact. The latter situation forces the computation to be terminated since the wall contact problem has not yet been incorporated.

The observed geometrical convergence behaviour is consistent with the behaviour predicted by (34) and indicates that the matrix of the coefficients $\alpha_{ij}$ is dominated by its diagonal elements which are negative.

Therefore we neglect the off-diagonal elements in (34) and thereby assume that the displacement variables geometrically approach their asymptotic values $V_i^{(\infty)}$ i.e.

$$V_i^{(n)} = V_i^{(\infty)} + A_{(i)}\alpha_{(ii)}^n \quad \text{as } n \to \infty; \text{ no summation on } i. \tag{36}$$

In the asymptotic regime, the coefficients $V_i^{(\infty)}$, $A_i$ and $\alpha_{(ii)}$ can be determined from the displacement values in three successive iterations. In particular, the asymptotic value for the displacement is given by

$$V_i^{(\infty)} = V_i^{(n+2)} - \frac{\left(V_i^{(n+2)} - V_i^{(n+1)}\right)^2}{V_i^{(n+2)} - 2V_i^{(n+1)} + V_i^{(n)}} \tag{37}$$

This equation is only valid in the asymptotic regime but numerical experiments showed that it is beneficial to apply the extrapolation as soon as possible, i.e. after every third iteration, since even the initial stages of the iteration tend to be well described by (36).

A further acceleration of the scheme in terms of computer time was achieved by exploiting the observation that the lubrication theory approximation of the Stokes equations[16] provides a good estimate of the pressure distribution in the flow. Therefore, the lubrication theory solver was used as the fluid solver in the first stage of the iteration. Once this iteration converged (in very little CPU time since the lubrication theory solution is much less computationally expensive than the full 3D Stokes solution) its equilibrium wall shape was used as the initial guess for the final iteration in which the Stokes solver was used. The overall procedure is summarised in the flowchart shown in Fig. 7.

Fig. 8 shows the convergence history for the same case as in Fig. 5 using the accelerated iteration procedure. The first stage of the iteration (based on the lubrication theory approximation for the fluid equations) converges in nine steps, applying the extrapolation procedure (37) twice. Then another five iterations with the Stokes solver suffice to produce the final converged solution.

It should be noted that the extrapolation procedure not only accelerates convergent iterations, but often makes otherwise divergent iterations converge. An example of this is shown in Fig. 9 where the basic iteration procedure leads to a situation in which the tube wall flip-flops between two extreme shapes. This phenomenon has been reported in previous investigations [10,11] in which it prevented the scheme's convergence in certain regions of parameter space. The non-convergent oscillatory behaviour corresponds to the case $\alpha_{ij} = -\delta_{ij}$. Only two applications of the extrapolation procedure are required to achieve convergence with the lubrication theory solver (see Fig. 10).

## 2.5 Validation and Performance

The shell solver was only slightly modified from the previous version which was documented in more detail in reference 16. The newly developed Stokes solver was tested by computing the flow through the undeformed tube (Hagen-Poiseuille flow). Furthermore, the numerical results for the flow through a slightly buckled tube were compared to the analytical results from a first order perturbation analysis. Excellent agreement between the analytical and numerical solutions was found[25]. Finally, the code was used to compute the flow through a moderately buckled tube and the predictions for the axial velocity component and the pressure distribution were compared to the predictions from the lubrication theory solver[16]. Good agreement was found, even for flows in tubes which were too strongly collapsed to properly justify the use of lubrication theory[25]. The overall conservation of mass was monitored by computing the volume flux through the upstream and downstream ends of the rigid tubes. Even for strongly collapsed tubes, the inflow and outflow rates differed by less than 0.1% from their theoretical value. Other tests included doubling the lengths of the rigid upstream and downstream tubes ($R_{up} = R_{down} = L_{up} = R_0$ and $L_{down} = 2R_0$ were used in the computations) to verify that the upstream and downstream boundary conditions did not affect the flow. The typical fluid and solid meshes are shown in Fig. 3. Typical discretisations involved 60 shell elements and approximately 1200 fluid elements, resulting in a total of approximately 500 and 30,000 degrees of freedom, respectively. For one test case this resolution was increased to ensure mesh independence of the solutions (a further refinement of the fluid mesh to approximately 89,000 degrees of freedom changed the fluid pressure distribution by less than $6.6 \times 10^{-3}$%). The code was originally developed on a DEC Alpha workstation and the final production runs were carried out on the Cray C90 at the Pittsburgh Supercomputing Center. The main computational cost is associated with the solution of the three-dimensional Stokes equations. The matrix-free evaluations of the matrix vector products required in the conjugate gradient iterations were carried out using sum factorisation techniques[26]. The procedure was optimised for the Cray vector architecture by pre-calculating the relevant quantities in (20) and (21) at the integration points and using a special node numbering scheme that enhanced vectorisation. The Stokes solver alone achieved a peak

performance of about 350 MFlop/s. The coupled solver typically executed at around 300 MFlop/s. About four to five hours of CPU time were required to trace an entire post-buckling deformation (from strong collapse with near opposite wall contact to the unbuckled axisymmetric tube). The convergence histories shown in Figs. 8 and 10 are fairly characteristic for the the scheme's behaviour in a wide range of parameters.

# 3 Results

In all computations $h/R_0 = 1/20$ and $\nu = 0.49$ were chosen to approximate the nearly incompressible behaviour of the relatively thick walled (by the standards of shell theory) rubber tubes typically used in the experiments mentioned above. Figure 11 shows a strongly collapsed tube subject to an external pressure of $p_{ext} = -p_\delta = 6.38 \times 10^{-4}$ and a volume flux which corresponds to $\bar{\mu} = 1.875 \times 10^{-6}$. The viscous flow through the most strongly collapsed part of the tube causes a large pressure drop in the fluid. This significantly increases the compressive load on the downstream end of the tube and forces two small regions on the side of the tube to buckle inwards as well. Fig. 12 shows the flow through three cross sections in the most strongly collapsed part of this tube. The contours indicate the magnitude of the axial velocity component and show that the flow is already beginning to split up into the two channels that will remain open when the opposite walls touch. The vectors represent the transverse velocity components and show the transverse flow changing its direction while passing through the point of strongest collapse. Further results, extensive parameter studies of the flow characteristics of the collapsible tube and a comparison with experimental results can be found in reference 25.

Finally, the bifurcation diagram shown in Fig. 13 illustrates the snap-through behaviour of the system as the control pressure, $p_\delta$, is varied. The diagram shows the radial displacement of two material points on the tube wall (at $\zeta^1 = 7.4$ and $\zeta^2 = 0, \pi/2$, respectively) versus the control pressure when the volume flux is held at a constant value ($\bar{\mu} = 1.875 \times 10^{-6}$). For large positive values of the control pressure $p_\delta$ (negative values of the external pressure, $p_{ext}$), the tube is completely inflated and it deforms axisymmetrically. Hence, both material points have the same radial displacements. As the control pressure is reduced (the chamber pressure increased), the transmural pressure at the tube's downstream end is reduced and becomes compressive. When this compressive transmural pressure exceeds a critical value, the axisymmetric deformation becomes unstable and the tube buckles – one of the material points collapses towards the tube's centreline (negative radial displacement) while the other one is displaced radially outward (positive radial displacement). The diagram shows that the buckling process is indeed subcritical: the loss of stability is accompanied by a sudden large change in the displacement field.

In a narrow range of control pressures, two solutions (one stable, the other one unstable) exist simultaneously. This raises the question if the solutions obtained in the present computations, in which the value of the control displacement is prescribed, are unique. In other words, for a given volume flux could there be multiple tube shapes with the same value of the control displacement? Numerical experiments suggest that this is not the case: the same solutions were obtained for different initial guesses (obtained by varying the magnitude of the pressure disturbance, $p_{cos}$, when generating the initial guess for the tube shape) and if different stepsizes were used in the incrementation of the control displacement.

It should be noted that the linear stability analysis in reference 14 shows that buckling modes with a higher number of circumferential waves exist. These represent further solutions and in this sense the solutions obtained here are not unique. However, according to the linear stability analysis the tube shapes with two circumferential waves are the only physically realisable ones since they have the lowest buckling pressure.

# 4 Conclusion

This paper has described the development of a fast and robust solver for a three-dimensional large-displacement fluid-structure interaction problem. The basic iterative approach (simple switching between fluid and solid solver) was accelerated by an extrapolation procedure based on the scheme's asymptotic convergence behaviour. A displacement control technique which was primarily implemented to overcome the convergence problems caused by the strong nonlinearities of the shell equations also proved necessary to stabilise the iteration procedure itself.

The further development of the scheme will have to address the following three areas: (i) extension to finite Reynolds number (ii) incorporation of the wall contact problem (iii) development of a stable time integration scheme for the unsteady problem based on the segregated approach. The extension to finite Reynolds number will be the most straightforward modification even though the solution of the non-linear Navier-Stokes equations will require a substantially larger amount of CPU time. It will be interesting to

investigate how the additional nonlinearity in the fluid equations will affect the convergence behaviour of the overall scheme. The incorporation of the wall contact problem is mainly a meshing problem since the topology of the fluid domain changes when opposite wall contact occurs. Finally, the development of a segregated time-dependent solver will be necessary to examine the large-displacement self-excited oscillations frequently observed in the experiments. A previous investigation of this problem in a two-dimensional geometry[13] revealed potential stability problems in the segregated time integration, indicating that further studies will be required before a three-dimensional version can be developed.

## Acknowledgements

The author wishes to thank Professor Roger Kamm, Dr. Serhat Yesilyurt and Dr. Naomi Chesler for many helpful discussions. Financial support for this project was provided by the German Academic Exchange Service (through a NATO fellowship). The computations were carried out at the Pittsburgh Supercomputing Center whose excellent support is gratefully acknowledged.

# References

1. Boderick, L.L. & Leonard, J.W., 'Nonlinear Response of Membranes to Ocean Waves Using Boundary and Finite Elements', *Ocean Engineering* **22**, 731-745 (1995).
2. Benney, R.J. & Stein, K.R., 'Computational Fluid-Structure Interaction Model for Parachute Inflation', *Journal of Aircraft* **33**, 730-736 (1996).
3. Hofer, M., Rappitsch, G., Perktold, K., Trubel, W.& Schima, H., 'Numerical Study of Wall Mechanics and Fluid-Dynamics in End-To-Side Anastomoses and Correlation to Intimal Hyperplasia', *Journal of Biomechanics* **29**, 1297-1308 (1996).
4. Perktold, K. & Rappitsch, G., 'Computer Simulation of Local Blood Flow and Vessel Mechanics in a Compliant Carotid Artery Bifurcation Model', *ASME Journal of Biomechanics* **28**, 845-856 (1995).
5. Perktold, K., Thurner, E. & Kenner, T., 'Flow and Stress Characteristics in Rigid Walled and Compliant Carotid-Artery Bifurcation Models', *Medical & Biological Engineering & Computing* **32**, 19-26 (1994).
6. Lou, Z., 'A Computer Simulation of the Blood Flow at the Aortic Bifurcation with Flexible Walls', *ASME Journal of Biomechanical Engineering* **115**, 306-315 (1993).
7. Kamm, R.D. & Pedley, T.J., 'Flow in Collapsible Tubes: A Brief Review', *ASME Journal of Biomechanical Engineering* **111**, 177-179 (1989).
8. Pedley, T.J., 'Longitudinal Tension Variation in Collapsible Channels: a New Mechanism for the Breakdown of Steady Flow', *ASME Journal of Biomechanical Engineering* **114**, 60-76 (1992).
9. Rast, M.P., 'Simultaneous Solution of the Navier-Stokes and Elastic Membrane Equations by a Finite-element Method', *International Journal for Numeric al Methods in Fluids* **19**, 1115 - 1135 (1994).
10. Lowe, T.W. & Pedley, T.J., 'Computation of Stokes Flow in a Channel with a Collapsible Segment', *Journal of Fluids and Structures* **9**, 885-905 (1995).
11. Luo, X.Y. & Pedley, T.J., 'Numerical Simulation of Steady Flow in a 2-D Collapsible Channel', *Journal of Fluids and Structures* **9**, 149-197 (1995).
12. Luo, X.Y. & Pedley, T.J., 'A Numerical Simulation of Unsteady Flow in a 2-Dimensional Collapsible Channel', *Journal of Fluid Mechanics* **314**, 191-225 (1996).
13. Shin, J.J., 'The Numerical Simulation of Flow Through Collapsible Channels', PhD Thesis. MIT (1996).
14. Heil, M., 'The Stability of Cylindrical Shells Conveying Viscous Flow', *Journal of Fluids and Structures* **10** , 173-196 (1996).
15. Heil, M., 'Large Deformations of Cylindrical Shells Conveying Viscous Flow', PhD Thesis. University of Leeds (1995).
16. Heil, M. & Pedley, T.J., 'Large Post-Buckling Deformations of Cylindrical Shells Conveying Viscous Flow', *Journal of Fluids and Structures* **10**, 565-599 (1996).
17. Heil, M. & Pedley, T.J., 'Large Axisymmetric Deformations of a Cylindrical Shell Conveying a Viscous Flow', *Journal of Fluids and Structures* **9**, 237-256 (1995).

18. Ghattas, O. & Li, X., 'A Variational Finite Element Method for Stationary Nonlinear Fluid-Solid Interaction', *Journal of Computational Physics* **121**, 347-356, (1995).

19. Cahouet, J. & Chabard, J.-P., 'Some Fast 3D Finite Element Solvers for the Generalized Stokes Problem', *International Journal for Numerical Methods in Fluids* **8**, 869-896 (1988).

20. Wempner, G., *Mechanics of Solids*, McGraw-Hill, New York 1977.

21. Bogner, F.K., Fox, R.L. & Schmit, L.A., 'A Cylindrical Shell Discrete Element', *AIAA Journal* **5**, 745-750 (1967).

22. Löhner, R., 'Design of Incompressible Flow Solvers: Practical Aspects'. In: *Incompressible Computational Fluid Dynamics. Trends and Advances.* (ed.: Gunzburger, M.D. & Nicolaides, R.A.) Cambridge University Press, Cambridge 1993.

23. Crisfield, M.A., 'A fast incremental/iterative solution procedure that handles "snap-through" ', *Computers & Structures* **13**, 55-62 (1991).

24. Keller, H.E., 'Numerical Solution of Bifurcation and Nonlinear Eigenvalue Problems'. In: *Applications of Bifurcation Theory.* (ed.: Rabinowitz, P.H.) Academic Press, New York 1977.

25. Heil, M., 'Stokes Flow in Collapsible Tubes – Computation and Experiment'. Accepted for publication in *Journal of Fluid Mechanics.*

26. Rønquist, E.M., 'Optimal Spectral Element Methods for the Unsteady Three-dimensional Incompressible Navier-Stokes Equations', PhD Thesis, MIT (1988).

# Appendix A: The Strain and Bending Tensors

The strain and bending tensors which describe the deformation of the shell in the variational principle (4) are obtained from the tangential base vectors to the deformed shell's midplane, $\mathbf{A}_\alpha = \mathbf{R}^0_{,\alpha}$. With the deformed midplane metric tensor $A_{\alpha\beta} = \mathbf{A}_\alpha \cdot \mathbf{A}_\beta$ the strain tensor is given by

$$\gamma_{\alpha\beta} = 1/2(A_{\alpha\beta} - \delta_{\alpha\beta})$$

since the undeformed midplane metric is orthogonal (the undeformed midplane metric tensor is $a_{\alpha\beta} = \delta_{\alpha\beta}$). With the normal vector to the deformed shell, $\mathbf{N} = \mathbf{A}_1 \times \mathbf{A}_2/|\mathbf{A}_1 \times \mathbf{A}_2|$, the non-dimensional curvature tensor of the deformed midplane is $B_{\alpha\beta} = \mathbf{N} \cdot \mathbf{A}_{\alpha,\beta}$. The non-dimensional bending tensor is given by

$$\kappa_{\alpha\beta} = -(B_{\alpha\beta} - b_{\alpha\beta}),$$

where the only non-zero entry in the undeformed curvature tensor $b_{\alpha\beta}$ is $b_{22} = -1$.

Many authors derived approximate shell theories in which different approximations to these exact strain and bending tensors were used. However, it was shown in reference 16, that the full non-linear expressions have to be retained to obtain accurate results in the large-displacement regime.

# Appendix B: The Uzawa Method

The solution of the discretised Stokes equations is based on the pressure equation (22) which is solved with a conjugate gradient iteration, preconditioned by the pressure mass matrix. The products of the pressure vector $\mathbf{p}$ with the matrix $\underline{\mathbf{G}} = \sum_{i=1}^{3} \underline{\mathbf{D}}_i \underline{\mathbf{A}}_i^{-1} \underline{\mathbf{D}}_i^T$, which are required during this iteration, are evaluated by an inner iteration since the formation of the matrix $\underline{\mathbf{G}}$ is computationally very expensive. The inner iteration evaluates $\underline{\mathbf{G}}\mathbf{p}$ by first computing the three auxiliary vectors $\mathbf{y}_i = \underline{\mathbf{D}}_i^T \mathbf{p}$ which are then used as the right hand sides in $\underline{\mathbf{A}}_i \mathbf{z}_i = \mathbf{y}_i$. These equations are solved with conjugate gradient iterations, preconditioned by the diagonals of the $\underline{\mathbf{A}}_i$. Finally, the required result is obtained from $\underline{\mathbf{G}}\mathbf{p} = \sum_{i=1}^{3} \underline{\mathbf{D}}_i \mathbf{z}_i$.

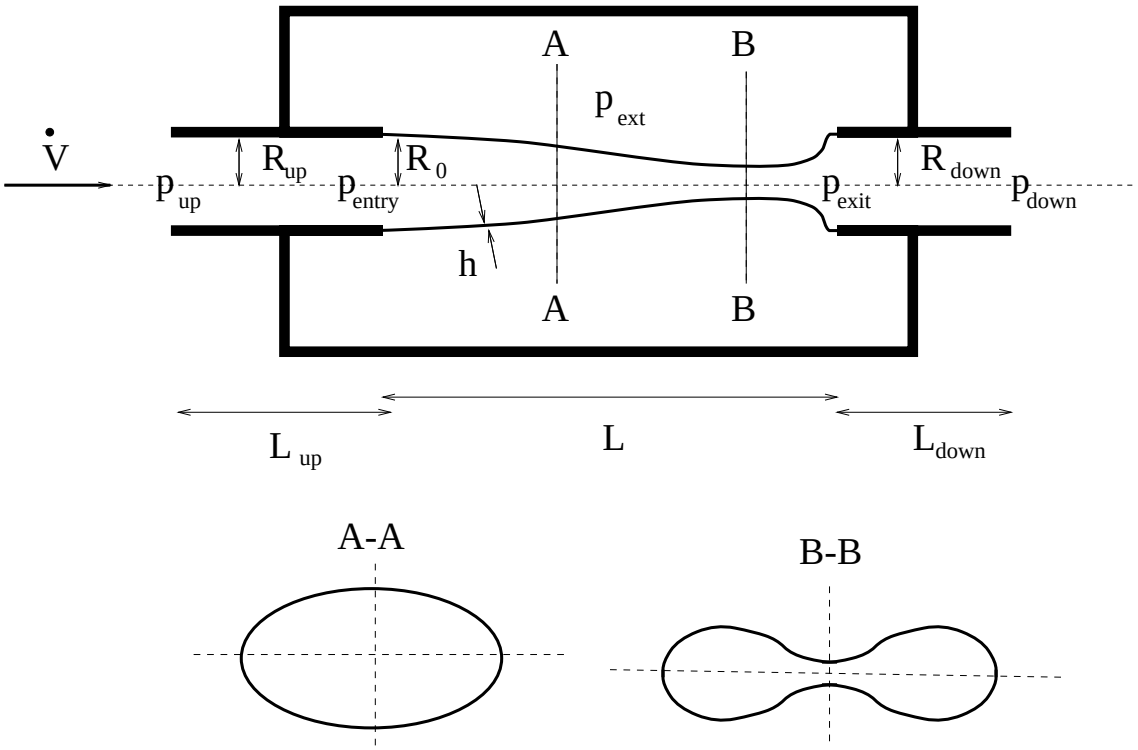


Figure 1: Sketch of the typical experimental setup.

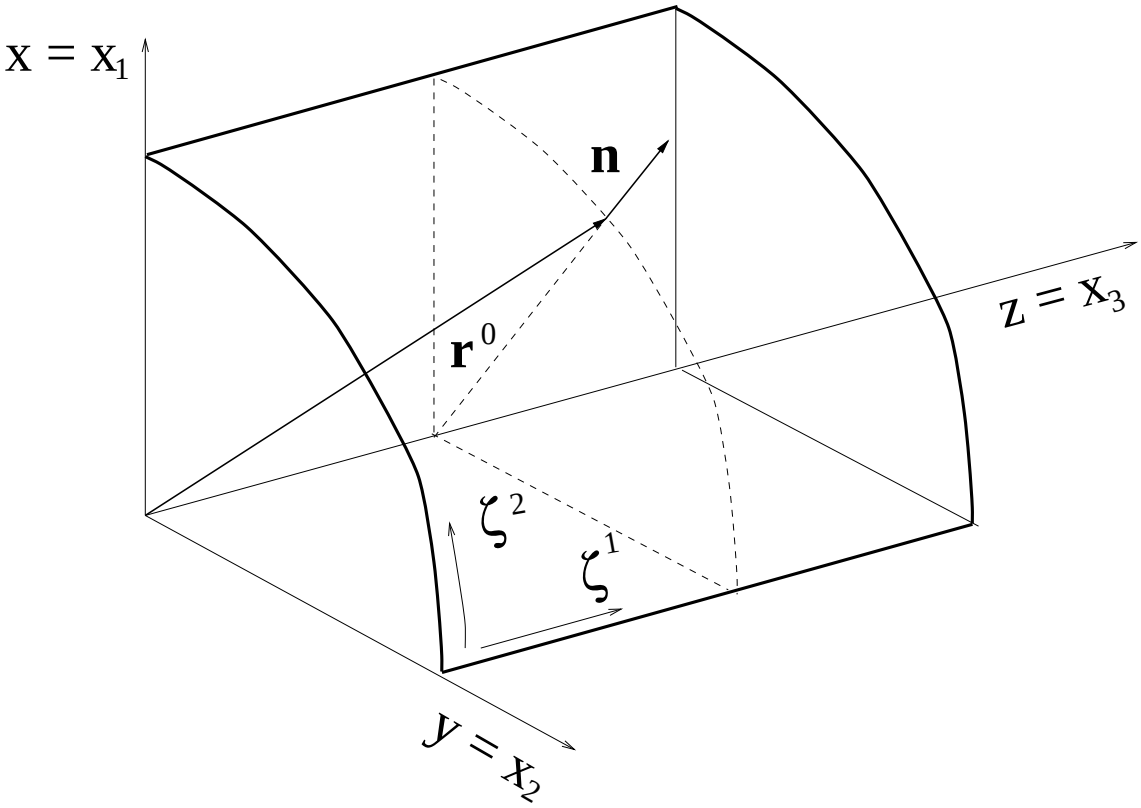


Figure 2: Sketch of the coordinate system used in the analysis.

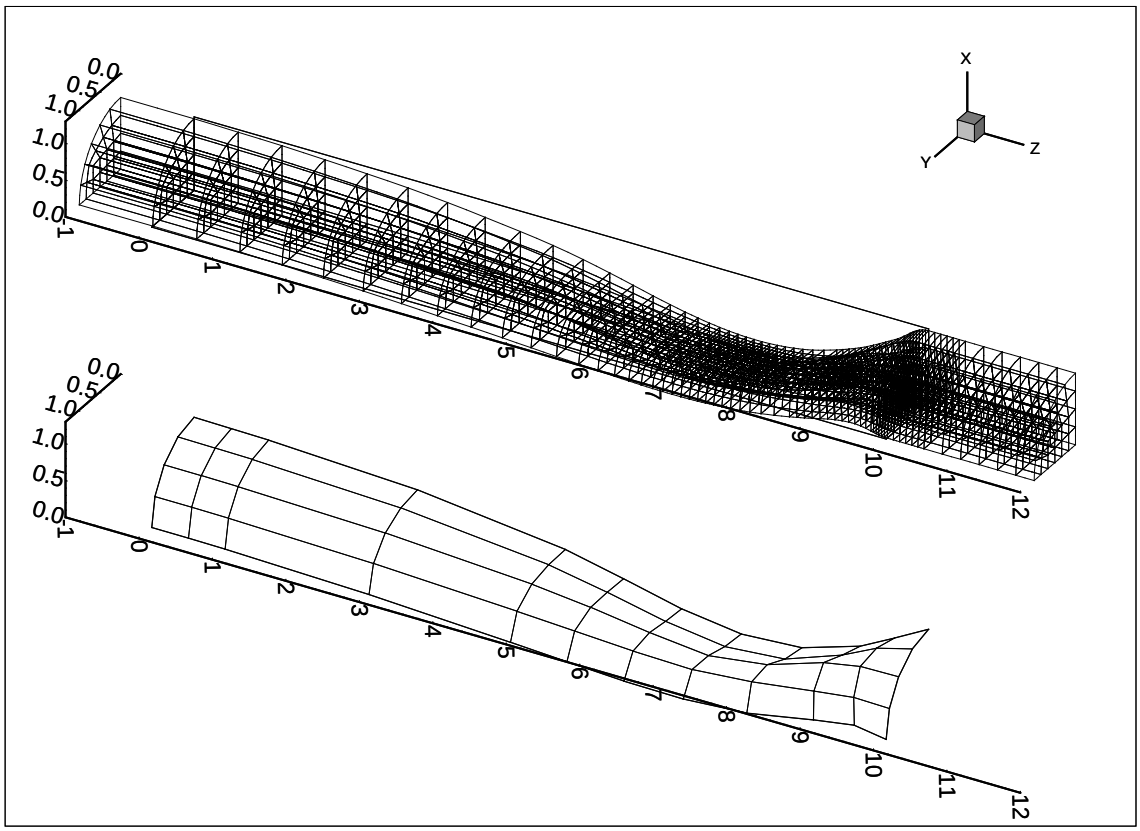


Figure 3: Fluid and solid meshes used for the Finite Element discretisation of the Stokes and shell equations. Only one quarter of the tube is discretised.

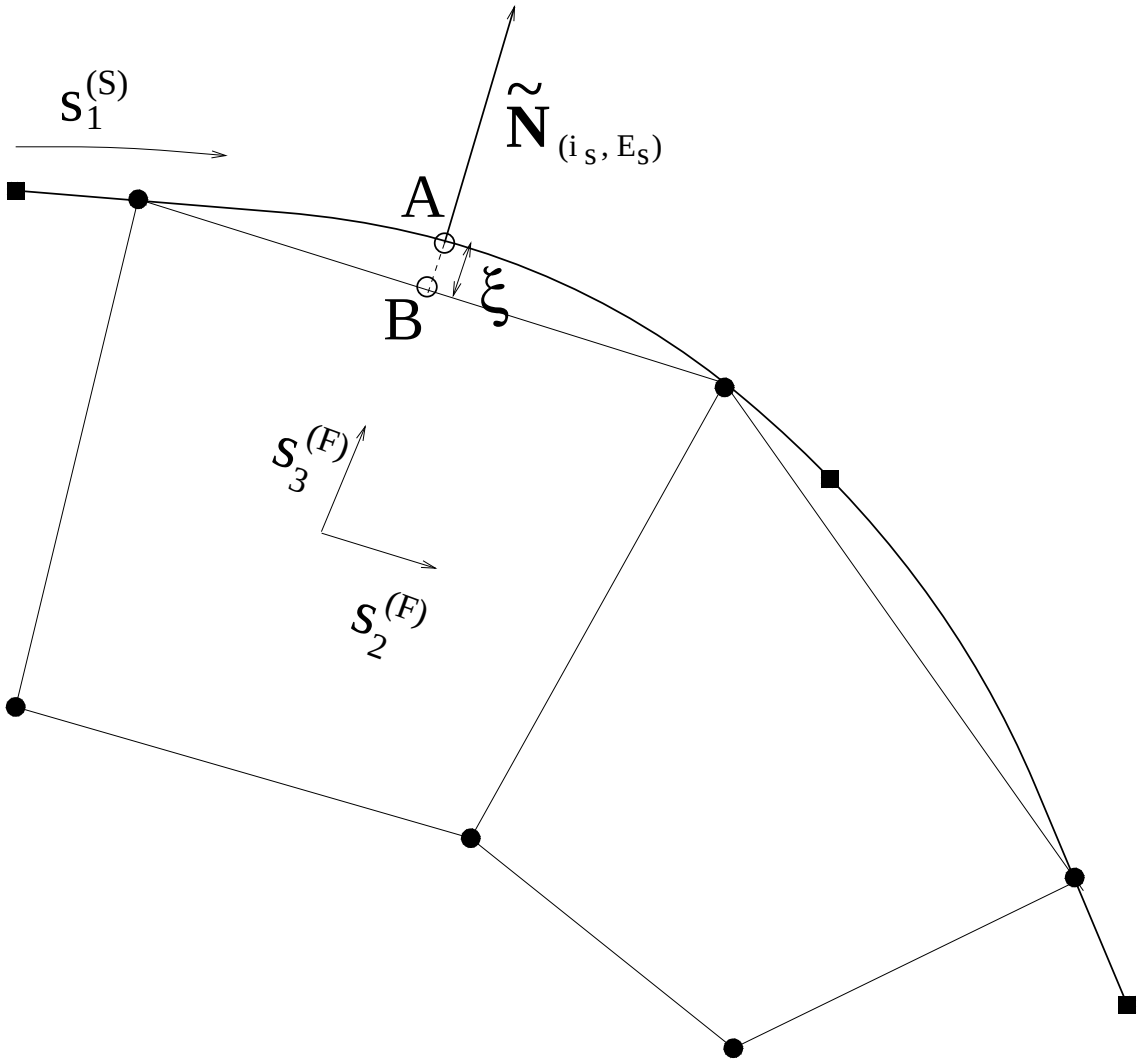


Figure 4: Sketch illustrating the transfer of the fluid traction from the discretised fluid domain to the FEM integration point in the solid domain. The solid squares and circles represent the corner nodes of the shell and fluid elements, respectively, and for simplicity the transfer is only illustrated for a two-dimensional geometry.

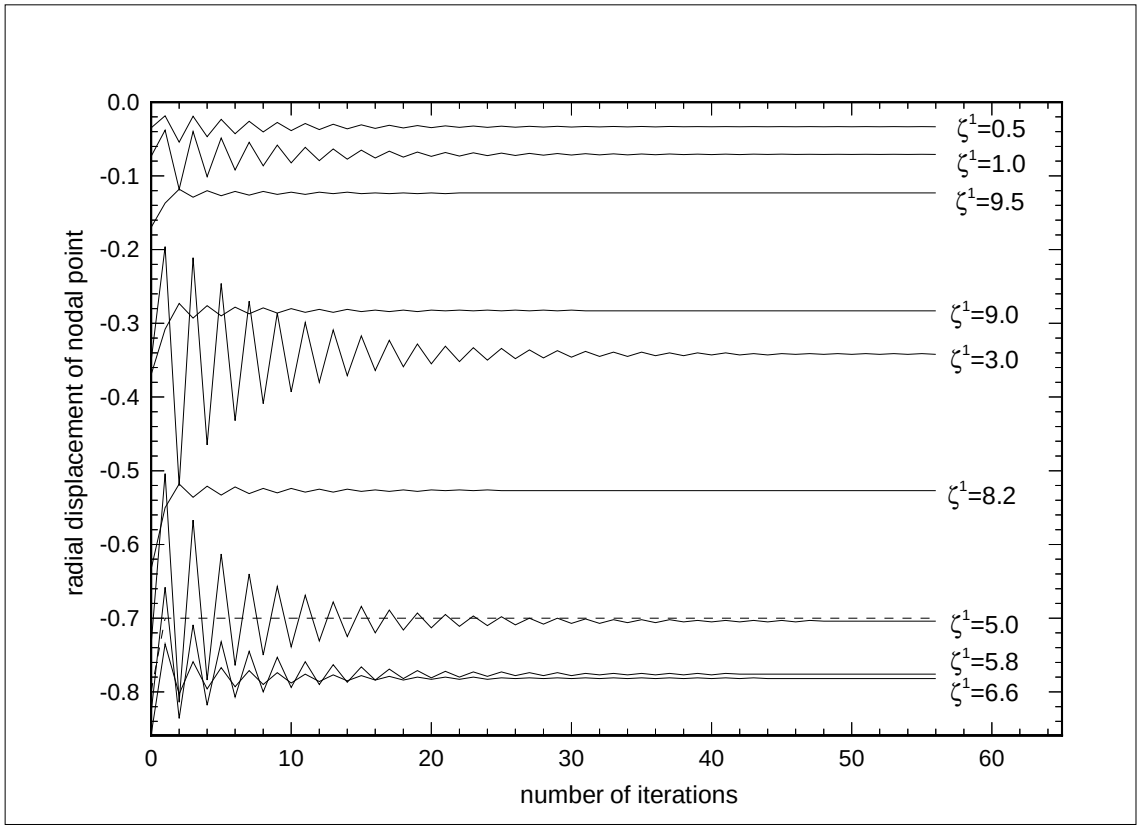


Figure 5: Displacement history of the nodal points on the material line $\zeta^2 = \pi/2$ during the Picard iteration. The dashed line shows the displacement of the control node (at $\zeta^1 = 7.4$). The control displacement is reduced from $\tilde{V} = -0.8$ to $\tilde{V} = -0.7$. $L/R_0 = 10,\ \bar{\mu} = 3.125 \times 10^{-7}$.

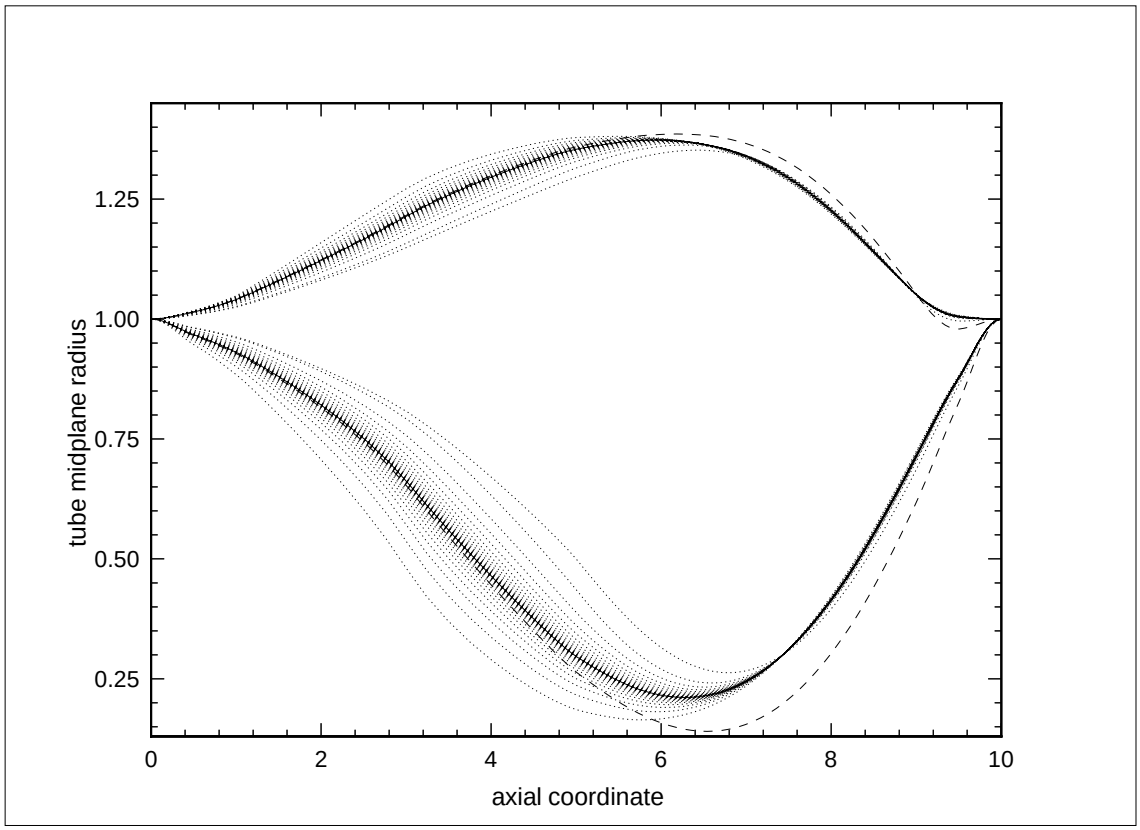


Figure 6: Displacement of the material lines $\zeta^2 = 0$ (bulging out) and $\zeta^2 = \pi/2$ (collapsing) during the Picard iteration. The dashed line shows the initial guess, the solid line is the final equilibrium shape and the dotted lines represent the intermediate tube shapes during the iteration. Note how the tube pivots around the control node at $\zeta^1 = 7.4$ and $\zeta^2 = \pi/2$. The control displacement is reduced from $\tilde{V} = -0.8$ to $\tilde{V} = -0.7$. $L/R_0 = 10,\ \bar{\mu} = 3.125 \times 10^{-7}$.

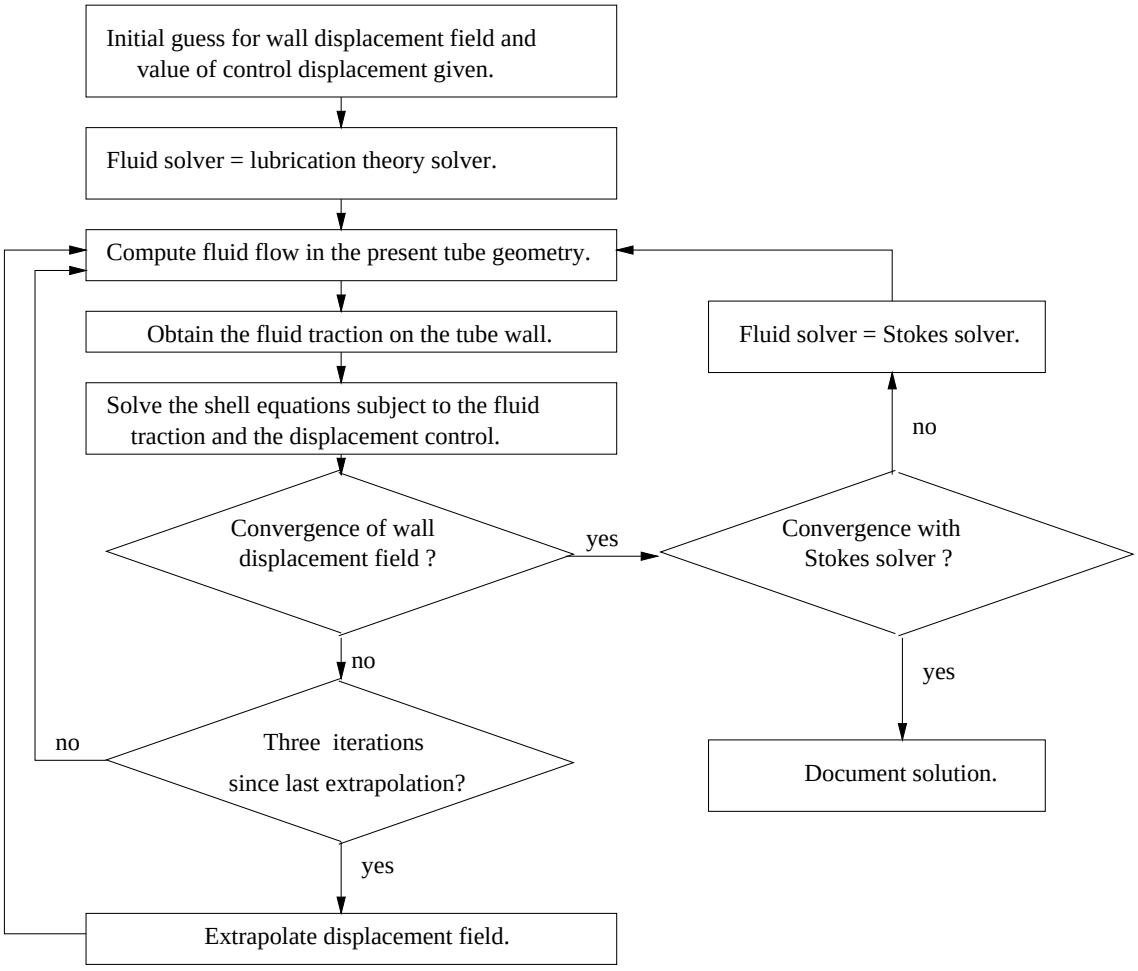


Figure 7: Flowchart summarising the accelerated iteration procedure. This procedure is embedded in an outer loop in which the value of the control displacement is varied to trace the entire range of the tube's collapse.

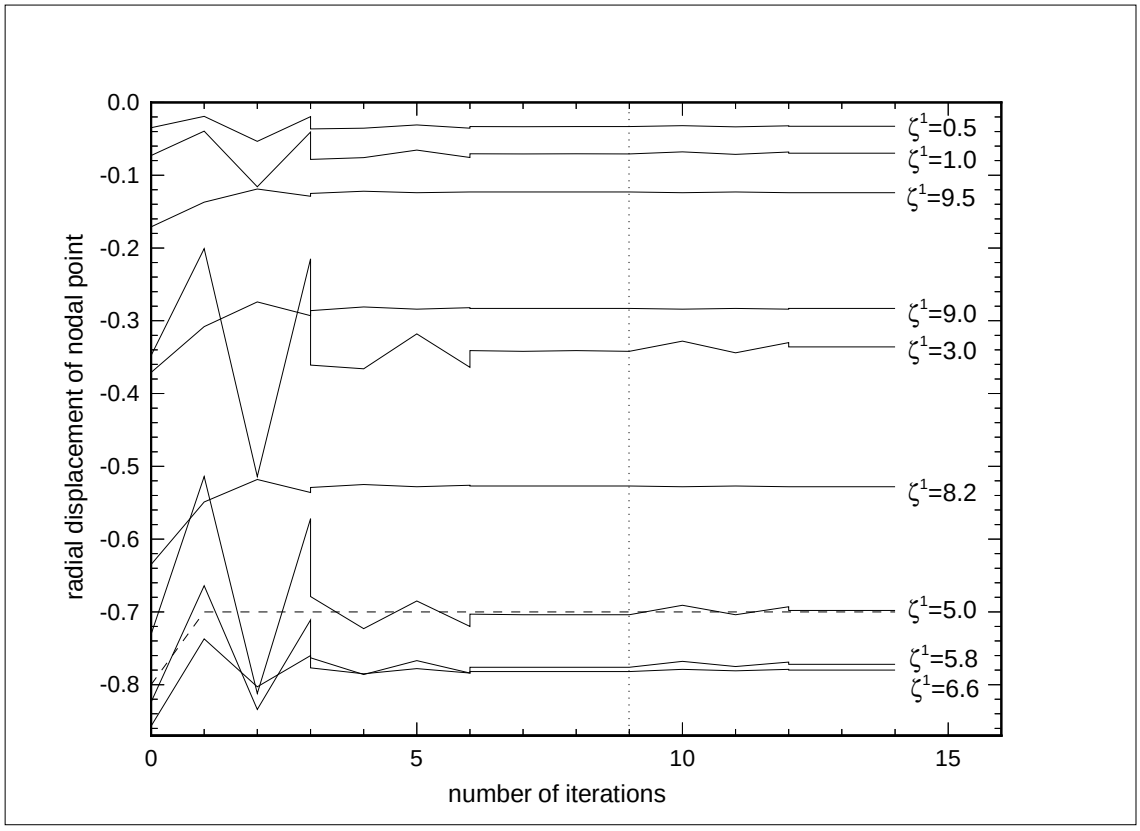


Figure 8: Displacement history of the nodal points on the material line $\zeta^2 = \pi/2$ during the accelerated Picard iteration. The iteration process begins with lubrication theory solves for the fluid equation. This iteration converges in nine steps (convergence marked by the vertical dotted line). With this initial guess only five Stokes solves are required to achieve a fully converged solution. The dashed line shows the displacement of the control node (at $\zeta^1 = 7.4$). The control displacement is reduced from $\tilde{V} = -0.8$ to $\tilde{V} = -0.7$. $L/R_0 = 10$, $\bar{\mu} = 3.125 \times 10^{-7}$.

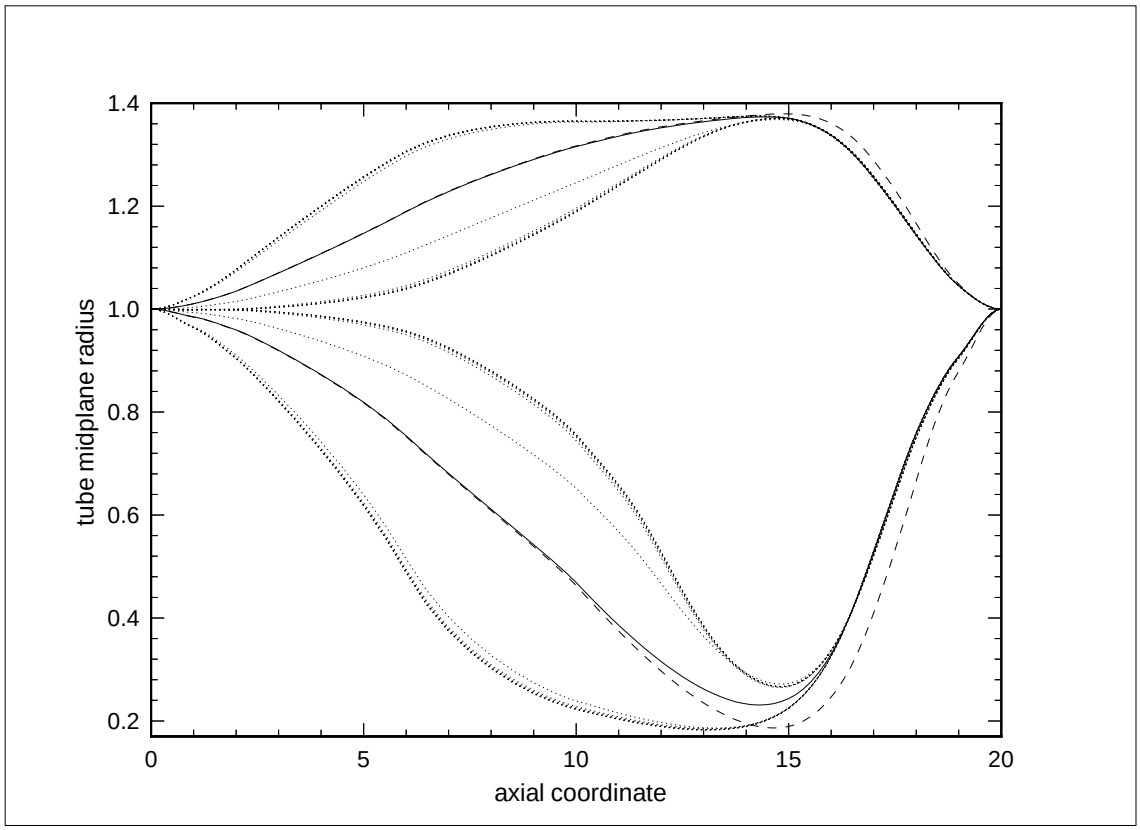


Figure 9: Displacement of the material lines $\zeta^2 = 0$ (bulging out) and $\zeta^2 = \pi/2$ (collapsing) during the Picard iteration. The dashed line shows the initial guess, the solid line is the equilibrium shape and the dotted lines represent the intermediate tube shapes during the iteration. The iteration fails to converge in spite of the good initial guess. The control displacement (at $\zeta^1 = 16.4$ and $\zeta^2 = \pi/2$) is reduced from $\tilde{V} = -0.7$ to $\tilde{V} = -0.6$. $L/R_0 = 20,\ \bar{\mu} = 6.25 \times 10^{-8}$.

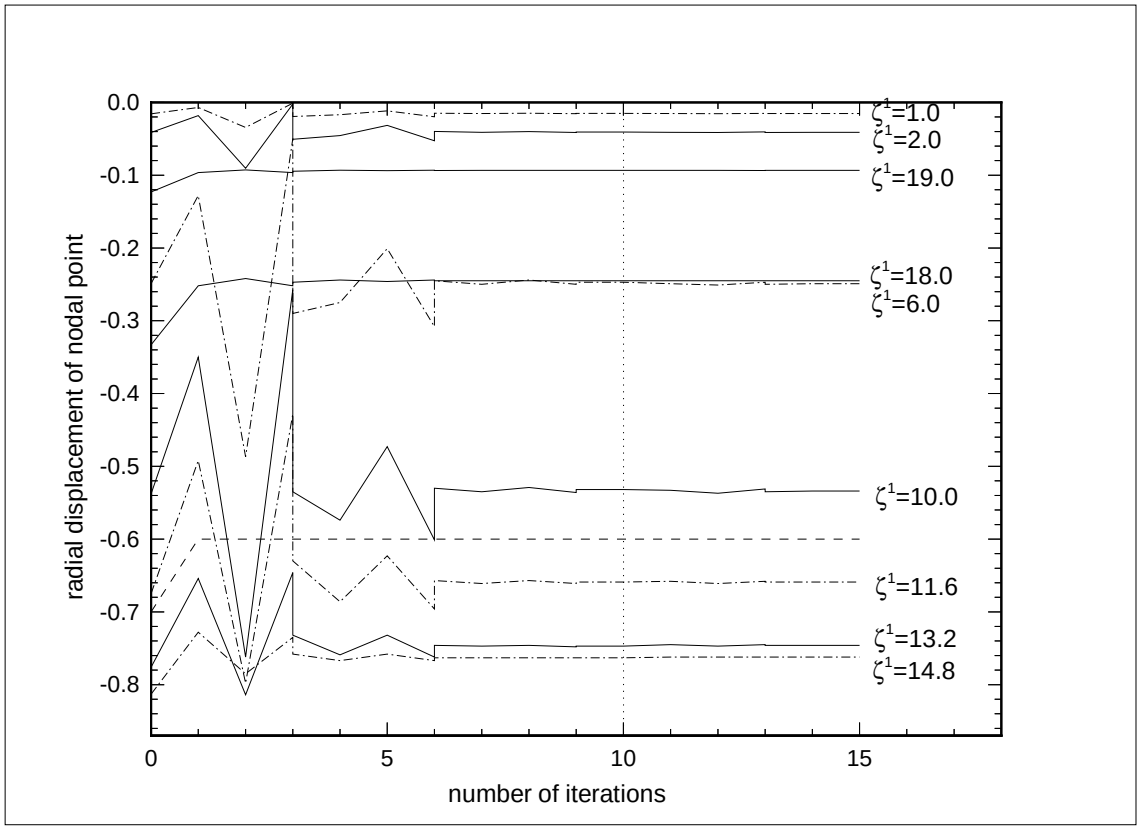


Figure 10: Displacement history of the nodal points on the material line $\zeta^2 = \pi/2$ during the accelerated Picard iteration (solid and dash-dotted lines). The dashed line shows the displacement of the control node (at $\zeta^1 = 16.4$). The extrapolation procedure stabilises the iteration procedure and achieves convergence with the lubrication theory solver after 10 iterations. Five iterations with the Stokes solver suffice to achieve a fully converged solution. The control displacement is reduced from $\tilde{V} = -0.7$ to $\tilde{V} = -0.6$. $L/R_0 = 20$, $\bar{\mu} = 6.25 \times 10^{-8}$.

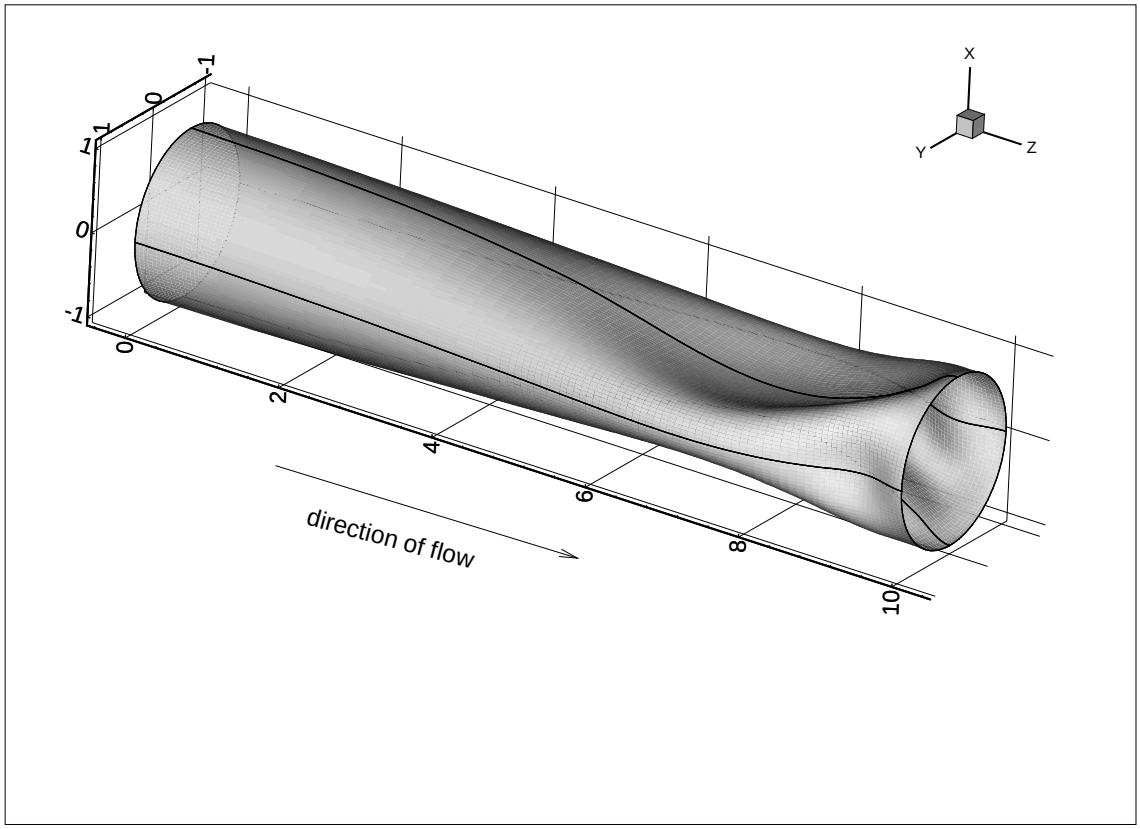


Figure 11: Strongly collapsed tube subject to $p_{ext} = 6.38 \times 10^{-4}$. $L/R_0 = 10$, $\bar{\mu} = 1.875 \times 10^{-6}$.

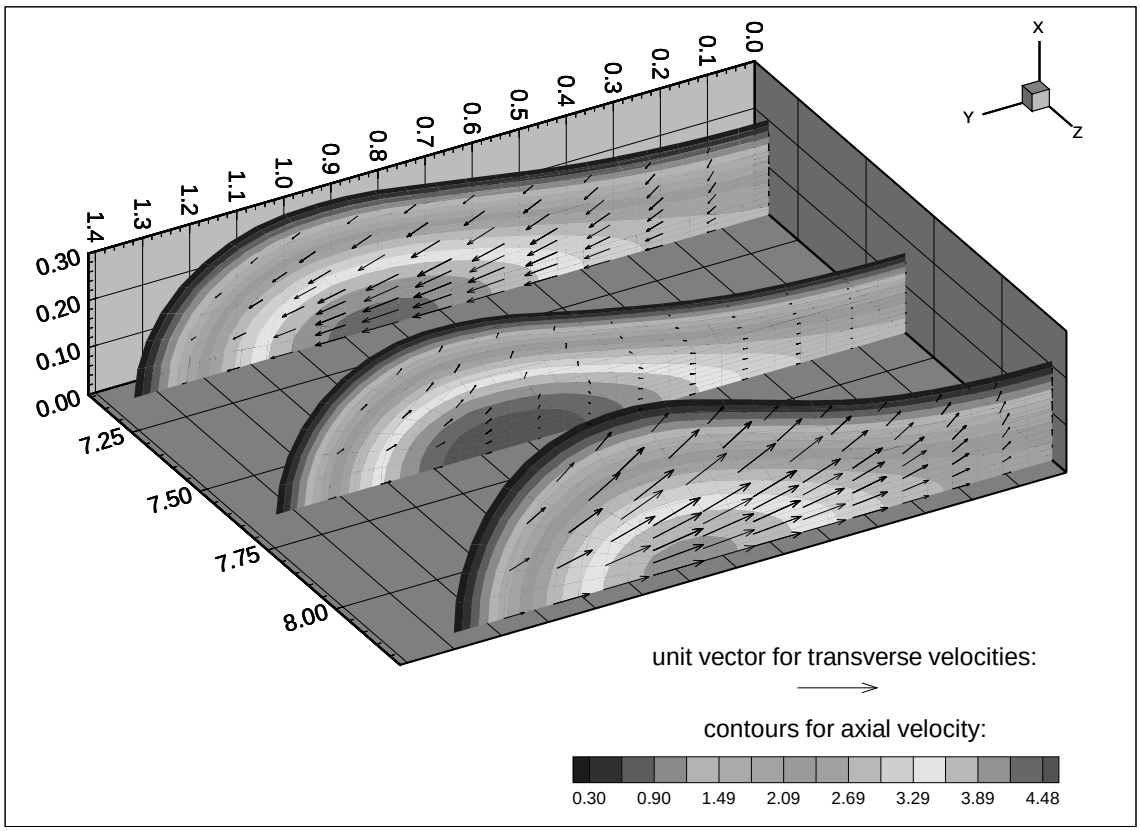


Figure 12: Flow through the strongly collapsed tube shown in the previous figure. Only one quarter of each cross section is shown. The contours indicate the magnitude of the axial velocity, the arrows represent the transverse velocity components. The cross sections are located at $z = 7.25,\ 7.75$ and $8.25$. $L/R_0 = 10,\ \bar{\mu} = 1.875 \times 10^{-6}$.

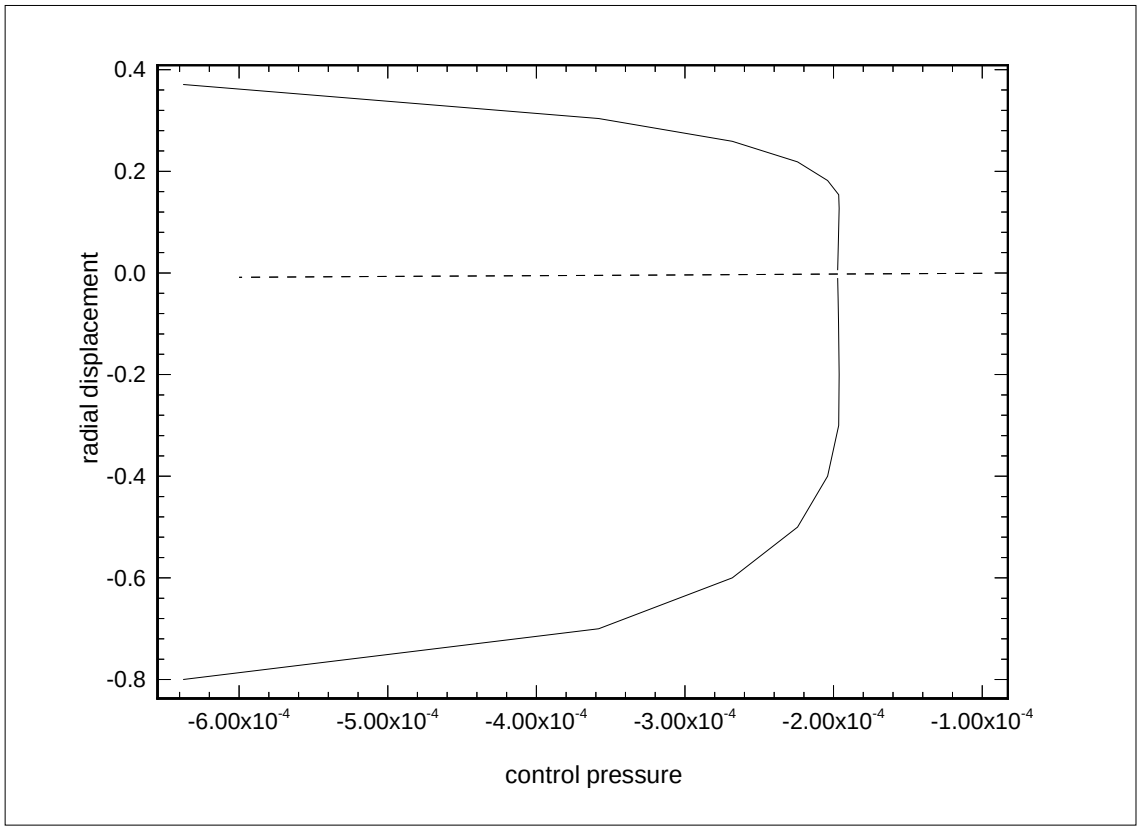


Figure 13: Bifurcation diagram, showing the tube deformation under constant volume flux ($\bar{\mu} = 1.875 \times 10^{-6}$). The radial deformation of two material points on the tube wall (at $\zeta^1 = 7.4$ and $\zeta^2 = 0, \pi/2$) is plotted as a function of the control pressure, $p_\delta$. The dashed line represents the axisymmetric pre-buckling deformation, the solid line represents the post-buckling solution.